Supporting Information for:

Far-Field Mid-Infrared Super-Resolution Imaging and Spectroscopy of Single High Aspect Ratio Gold Nanowires

Kyle Aleshire,[a] Ilia M. Pavlovetc,[a] Robyn Collette,[b] Xiang-Tian Kong,[c] Philip D. Rack,[b,d] Shubin Zhang,[e] David J. Masiello,[c] Jon P. Camden,[a] Gregory V. Hartland,[a,*] Masaru Kuno[a,e,1]

a. *Department of Chemistry and Biochemistry, University of Notre Dame, Notre Dame, IN, 46556*

b. *Department of Materials Science and Engineering, University of Tennessee, Knoxville, TN, 37996*

c. *Department of Chemistry, University of Washington, Seattle, WA, 98195*

d. *Center for Nanophase Materials Science, Oak Ridge National Laboratory, Oak Ridge, TN, 37831*

e. *Department of Physics, University of Notre Dame, Notre Dame, IN, 46556*

---

[1] Corresponding authors: Gregory V. Hartland and Masaru Kuno
  Emails: ghartlan@nd.edu and mkuno@nd.edu

1. Additional Experimental Data

Scanning electron microscopy (SEM) images, visible extinction spectrum of a single nanowire and additional infra-red photothermal heterodyne imaging (IR-PHI) images are presented in **Figures S1 – S3**. The SEM images show that the dimensions of the nanowires can vary from the specified dimensions in the CAD drawings used in the nanofabrication process, and that there is a significant amount of surface roughness associated with the nanowires.
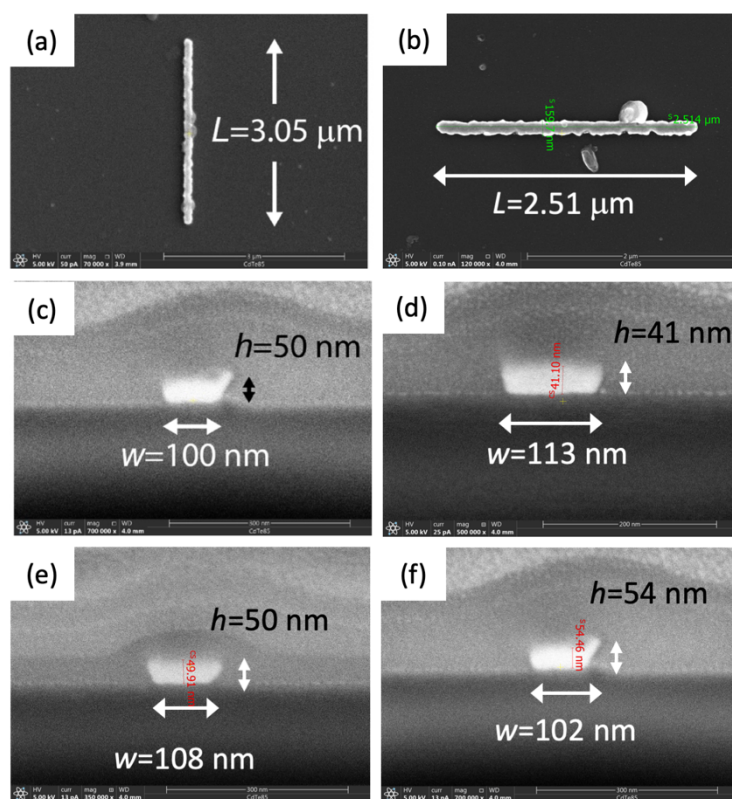
Figure S1: Representative scanning electron micrographs of individual Au nanowires. Panels (a) and (b) present low magnification images showing the nanowire lengths. The target lengths for the nanowires in panels (a) and (b) were 3.05 μm and 2.50 μm, respectively. Panels (c) – (f) present cross sectional images of the nanowires showing their width and height.
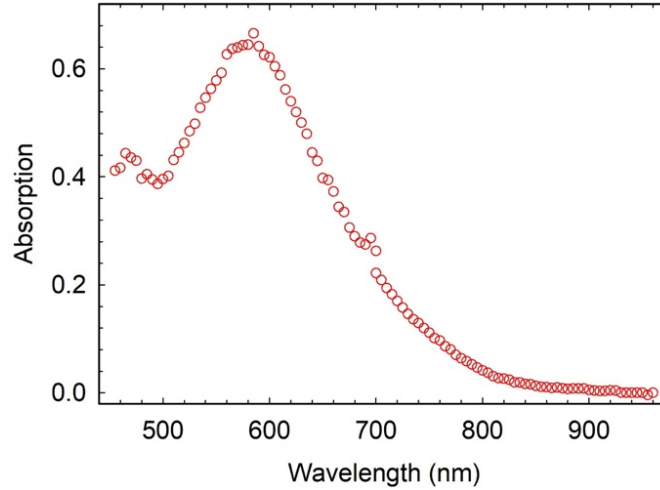
Figure S2: Representative visible extinction spectrum of a single Au nanowire. The peak at 600 nm is assigned to the transverse localized surface plasmon resonance of the nanowire. The break at ~690 nm is due to the acousto-optical tunable filter used with the supercontinuum source.
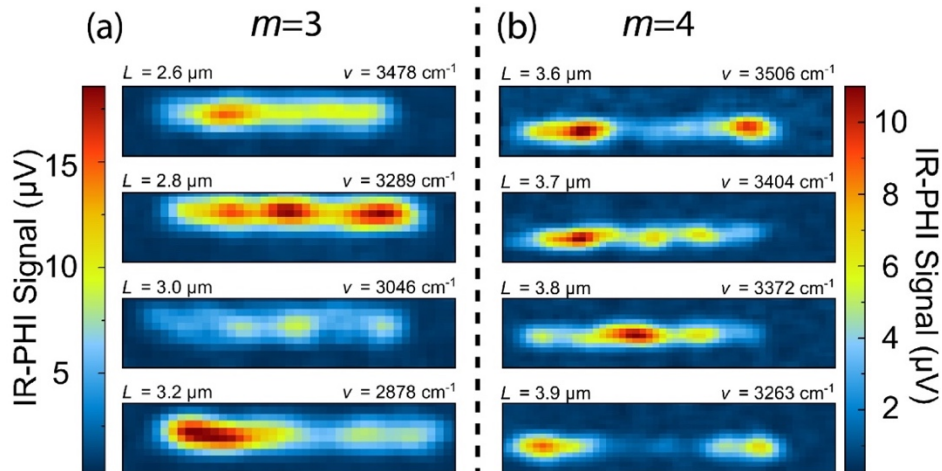
Figure S3: Additional (a) $m = 3$ and (b) $m = 4$ IR-PHI plasmon maps for nanowires with lengths L of (a) $L = 2.6$ to 3.2 μm and (b) $L = 3.6$ to 3.9 μm.

2. Finite Element Simulations

Three-dimensional finite element method (FEM) simulations of the nanowire absorption and the subsequent heat diffusion process are performed using COMSOL Multiphysics. Meshes of nonuniform sizes are used in the FEM calculations: the maximum sizes of the mesh in the metal and surrounding materials are 8 nm and 40 nm, respectively. Boundary layers of meshes are generated in the metal domain to account for the very thin penetration depth of mid-IR waves in metals. The geometry of the wire is modelled as a rectangular cross section (100 nm × 50 nm, see **Figure S1**), with the edges rounded with a 5 nm radius to avoid generation of very dense meshes near the corners and to facilitate the FEM calculations. The Helmholtz equation for the electromagnetic calculations and the heat diffusion equation are solved using the same mesh, except that additional perfect matched layers are used in the electromagnetic calculations to absorb the scattered light going out of the computation domain. **Figure S4** shows a diagram of the geometry used for the electromagnetic calculations. Simulations are performed at incident angles of ± 15° to approximate the range of angles created by the focusing objective in the experiments.
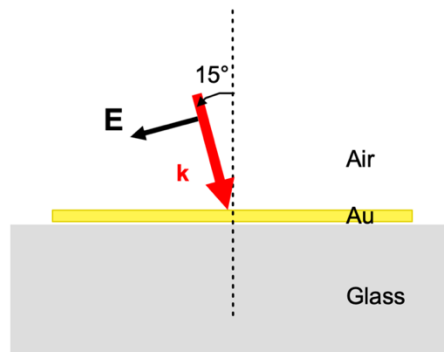

Figure S4: Diagram of the geometry used for the FEM simulations. The permittivity of glass was chosen to be 2.45, and the Johnson and Christy values were used for the wavelength dependent permittivity of gold (Ref. (1))

For the simulated spectra and absorption images presented in the main text, and for **Figure S5** below, FEM simulations performed at incident angles of +15° and -15° are averaged together. This models symmetrical excitation, which is expected when the Cassegrain objective is well aligned. The main text shows FEM simulation maps of the resistive heating and time-dependent temperature changes for the $m = 3$ and $m = 4$ Fabry-Pérot modes of a 3.1 μm long Au nanowire on a glass substrate for symmetrical excitation. In **Figure S5** corresponding data is presented for a 3.8 μm long nanowire. Simulations were also performed for unsymmetrical excitation, that is, only with a +15° angle of incidence. This models the case where the Cassegrain is miss-aligned, so that the IR excitation beam does not evenly illuminate the sample. The results of these simulations are presented in **Figures S6** and **S7**. Note that in all the image simulations the excitation wavelength is chosen to be at the maximum for each resonance, and the temperature profiles in the right-hand panels of the figures have been offset for clarity.
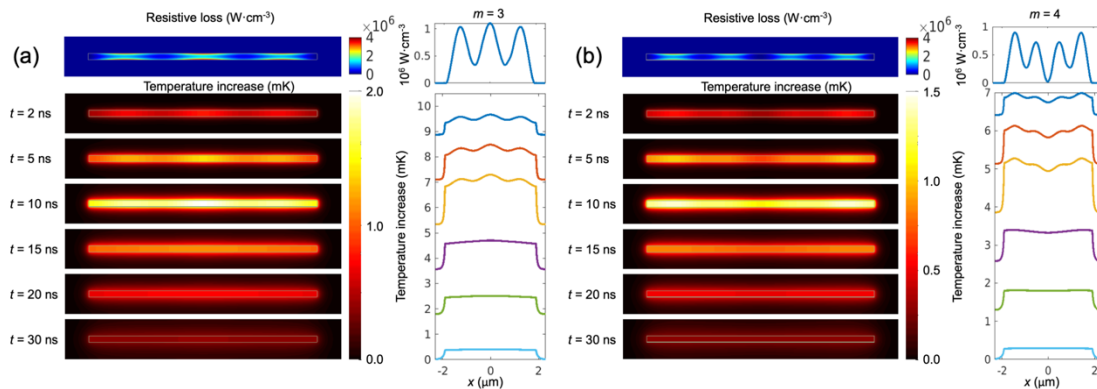
Figure S5: FEM simulation maps of the resistive heating (top) and time-dependent temperature changes (bottom) for a 3.8 μm long Au nanowire on a glass substrate for (a) $m = 3$ and (b) $m = 4$ Fabry-Pérot modes for symmetric excitation (± 15° excitation).
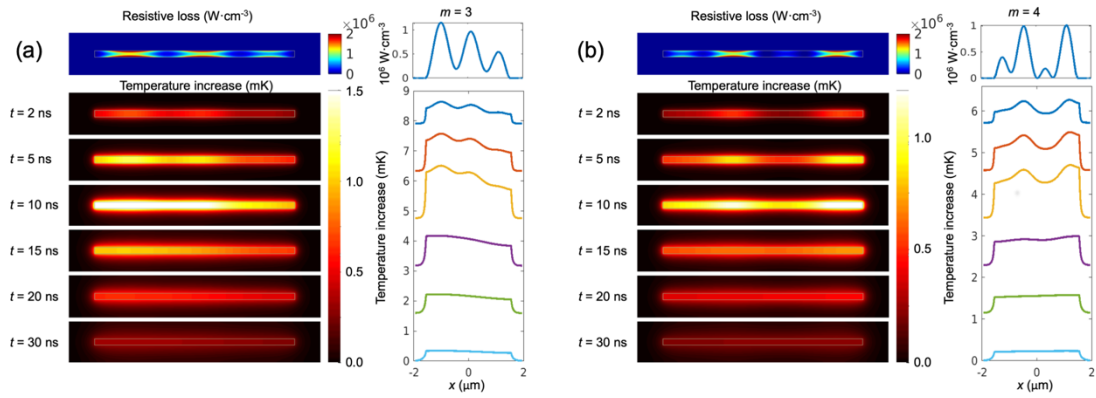
Figure S6: FEM simulation maps of the resistive heating (top) and time-dependent temperature changes (bottom) for a 3.1 μm long Au nanowire on a glass substrate for (a) *m* = 3 and (b) *m* = 4 Fabry-Pérot modes for unsymmetrical excitation (only +15° excitation).
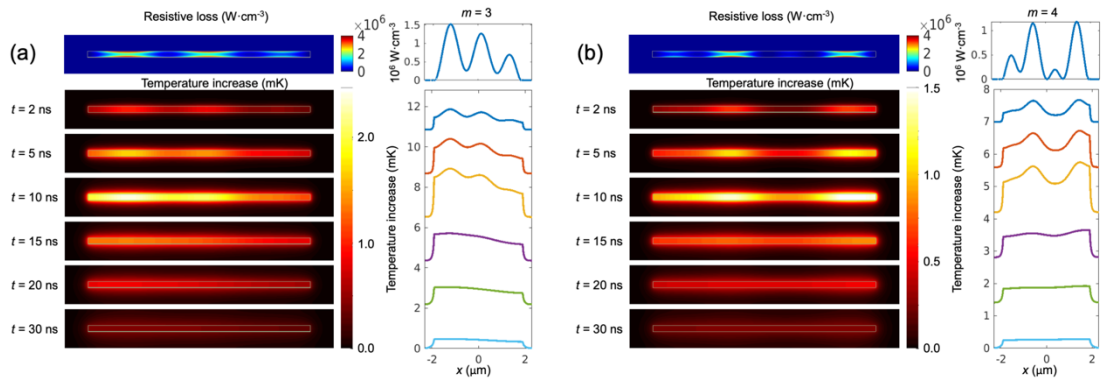

Figure S7: FEM simulation maps of the resistive heating (top) and time-dependent temperature changes (bottom) for a 3.8 μm long Au nanowire on a glass substrate for (a) *m* = 3 and (b) *m* = 4 Fabry-Pérot modes for unsymmetrical excitation (only +15° excitation).

It is interesting to note that the plasmon mode structure for asymmetric excitation (**Figures S6** and **S7**) is also asymmetric. As discussed in the main text, this offers a possible explanation for the observation of asymmetry in the experimental images, see **Figure S3** for examples.

FEM simulations were also used to estimate the effective index n_{eff} for Equation 1 of the main text. A two-dimensional mode analysis calculation was performed in COMSOL for rectangular structures on a glass surface. These calculations yield the complex effective mode index for the system $\tilde{n} = n_{eff} + i\,\alpha/k_0$.(2-7) The real part of $\tilde{n}$ gives the wavevector $k_{SPP} = n_{eff}k_0$ for the propagating surface plasmon polariton (SPP) modes of the structure, and the imaginary part is related to the propagation length by $L_{SPP} = 1/2\alpha$. Note that the 2D simulations correspond to infinitely long nanostructures. **Figure S8(a)** shows an image of the field distribution for the SPP modes found in the analysis, and **Figure S8(b)** displays the dispersion curve for the mode for the frequency range of interest in the experiments. The effective index for the SPP mode varies from 1.55 to 1.72, respectively, over the 2.5 to 3.5 μm wavelength range of the experiments, with a value of 1.63 at 3 μm (approximately the middle of the experimental wavelength range). These values of n_{eff} are consistent with the value of $n_{eff} = 1.64$ derived from fitting the resonance frequency versus m/L data in **Figure 2(a)** of the main text.
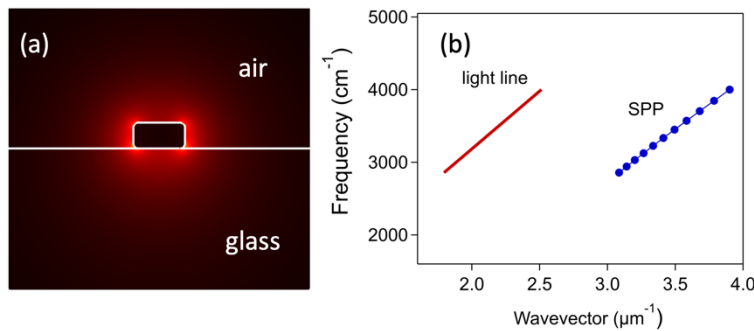
Figure S8: (a) Mode plot (norm of the electric field) for the SPP mode supported by an infinitely long, rectangular Au nanowire. The free space wavelength was 3 μm, and the value of the refractive index of the glass was 1.49. (b) Dispersion curve for the SPP mode (blue symbols) and for free space photons (red line).

The slope of the dispersion curve in **Figure S8(b)** gives the group velocity of the SPP mode $(v_g = (\partial\omega/\partial k))$, which can be combined with L_{SPP} to calculate the plasmon lifetime by $T_1 = L_{SPP}/v_g$.(8) We find $v_g = 0.88c_0$ and $T_1 = 21$ fs for SPPs in the mid-IR. This yields a dephasing time of $T_2 = 2T_1 = 42$ fs, and a corresponding dephasing rate of $\Gamma = 2\hbar/T_2 = 31$ meV. Interestingly, the dephasing rate from this simple calculation is well below the Drude limit of 78 meV,(1) and is similar to the measured and calculated dephasing rates for the resonances reported in the main text. This indicates that the two-dimensional FEM simulations capture the field deconfinement effects that are responsible for the reduced linewidths in the mid-IR region.

References:

1. P. B. Johnson, R. W. Christy, Optical constants of the noble metals. *Phys. Rev. B* **6**, 4370-4379 (1972).
2. R. Zia, M. D. Selker, M. L. Brongersma, Leaky and bound modes of surface plasmon waveguides. *Phys. Rev. B* **71**, 165431 (2005).
3. J. Jung, T. Søndergaard, S. I. Bozhevolnyi, Theoretical analysis of square surface plasmon-polariton waveguides for long-range polarization-independent waveguiding. *Phys. Rev. B* **76**, 035434 (2007).
4. M. Song *et al.*, Imaging symmetry-selected corner plasmon modes in penta-twinned crystalline Ag nanowires. *ACS Nano* **5**, 5874-5880 (2011).
5. S. P. Zhang, H. X. Xu, Optimizing substrate-mediated plasmon coupling toward high-performance plasmonic nanowire waveguides. *ACS Nano* **6**, 8128-8135 (2012).
6. P. Johns, G. Beane, K. Yu, G. V. Hartland, Dynamics of surface plasmon polaritons in metal nanowires. *J. Phys. Chem. C* **121**, 5445–5459 (2017).
7. H. Wei *et al.*, Plasmon waveguiding in nanowires. *Chem. Rev.* **118**, 2882-2926 (2018).
8. T. Devkota, B. S. Brown, G. Beane, K. Yu, G. V. Hartland, Making waves: Radiation damping in metallic nanostructures. *J. Chem. Phys.* **151**, 080901 (2019).